
Investigation of the characteristics of low-level jets over North America in a convection-permitting WRF simulation

Xiao Ma^{1,2}, Yanping Li^{1,2}, Zhenhua Li¹, Fei Huo¹

¹Global Institute for Water Security, University of Saskatchewan, 11 Innovation Blvd, Saskatoon, SK, S7N 3H5, Canada

²School of Environment and Sustainability, University of Saskatchewan, 117 Science Place, Saskatoon, SK, S7N 5C8, Canada

Correspondence to: Yanping Li (yanping.li@usask.ca)

Abstract. In this study, we utilized a high-resolution (4 km) convection-permitting Weather Research Forecasting (WRF) simulation spanning a 13-year period (2000-2013) to investigate the climatological features of Low-level Jets (LLJs) over North America. The 4-km simulation enabled us to represent the effects of orography and the underlying surface on the boundary layer winds better. Focusing on the continental US and the adjacent border regions of Canada and Mexico, this study not only identified several well-known large-scale LLJs such as the southerly Great Plains LLJ and the summer northerly California coastal LLJ, but also the winter Quebec northerly LLJ which gets less focus before. All these LLJs reach the strongest in the night time in the diurnal cycle. Thus, the different thermal and dynamic mechanisms forming these three significant LLJs are investigated in this paper: Inertial oscillation theory dominates in Great Plain LLJ, California coastal LLJ is formed by the baroclinic theory, whereas the Quebec LLJ is associated with both theories. Moreover, the high-resolution simulation revealed climatic characteristics of weaker and smaller-scale LLJs or low-level wind maxima in regions with complex terrains, such as the northerly LLJs in the foothill regions of the Rocky Mountains and the Appalachian during the winter. This study provides valuable insights into the climatological features of LLJs in North America and the high-resolution simulation offers a more detailed understanding of LLJ behavior near complex terrains and other smaller-scale features.

25 1. Introduction

26 A low-level jet (LLJ) is described as the fast-moving air ribbon located in the lower atmosphere most of the time
27 (Bonner, 1968; Rife et al., 2010). Many of the world's LLJs have been studied, such as the Great Plains LLJ over the
28 central US (Bonner, 1968; Zhong et al., 1996), the Somali LLJ over eastern Africa (Munday et al., 2021), and the
29 South American LLJ over the east Andes Mountains (Montini et al., 2019). Other studies extend beyond in-land LLJs
30 to encompass offshore coastal LLJs such as the California LLJs (Parish, 2000) and North African Coastal LLJ (Soares
31 et al., 2018). A kind of mesoscale weather system, an LLJ has a relatively small vertical range of usually only a few
32 hundred meters, but its width can reach several hundred kilometers. LLJs are closely related to precipitation and even
33 extreme events, and they can transfer abundant water vapor to the downwind regions, providing favorable dynamic
34 conditions for rainfall (Walters and Winkler, 2001; Hodges and Pu, 2019). Meanwhile, researchers have long been
35 interested in investigating their features, because LLJs also affect various processes such as wind power development,
36 air pollution transportation, and urban heat islands: the wind turbines would be influenced by positive wind shear and
37 downward entrainment from the LLJs above them, assisting in extracting energy from the strong wind belt inside LLJs
38 (Gadde and Stevens 2021; Ma et al., 2022). LLJ-related horizontal transportation is beneficial to pollutant removal
39 (Sullivan et al. 2017). The LLJs can enhance the turbulent mixing in the boundary layer thereby decreasing the
40 atmospheric stability, helping pollution diffusion, and weakening urban heat island intensity (Hu et al., 2013).

41 Since the mid-20th century, scientists have used regular rawinsonde observations to investigate the characteristics of
42 LLJs. Applying rawinsondes to investigate the Great Plains LLJ in the central US, Bonner (1968), Mitchell et al.
43 (1995), and Walters et al. (2008) studied its distribution, seasonal activity, horizontal and vertical structure, and diurnal
44 features and established the climatology of the Great Plains LLJ during warm seasons. As well as rawinsondes, radar
45 systems and wind profilers are useful tools for characterizing LLJs. Frisch et al. (1992) observed a typical LLJ process
46 using Doppler weather radar in North Dakota and identified that the friction on the surface of the boundary layer is
47 important in the early stages of LLJ development. Using long-term wind profiler measurement, Miao et al. (2018)
48 interpreted the climatology of LLJs in Beijing and Guangzhou, concluding that the frequency values of LLJs in these
49 two cities are 13.0% and 4.9%, respectively. Moreover, Smith et al. (2019) used the Plains Elevated Convection at
50 Night (PECAN) observations to conduct high-quality measurements of nocturnal LLJs with wide spatial and temporal
51 resolutions. They found that sudden changes in LLJ structure typically result from the spatial evolution of the LLJ.

52 However, there are some disadvantages of observational research that should be noted. First, regular rawinsonde data
53 only contain measurements at two daily time points (00 UTC and 12 UTC), which cannot fully capture LLJs' diurnal
54 variations. The time density of observations is therefore coarse, and coastal areas lack regular high-density
55 measurements, making the study of coastal LLJs challenging (Mitchell et al., 1995). Second, heterogeneities in the
56 rawinsonde records, such as variations in station locations, radiosonde types, and archiving procedures, may also
57 complicate the use of these observations in climate research. Third, rawinsonde measurements taken at a single point
58 are not able to capture horizontal shear and environmental conditions (Chen et al., 2005). Although observation
59 platforms such as radar, PECAN, or lidar which investigate the atmosphere as low as 300 m, can compensate to some
60 extent for this lack of observational data. as well as lidar that investigates the atmosphere as low as 300 m, these
61 approaches are still limited by the spatial coverage of their measurement platforms (Smith et al., 2019).

62 Because of these problems with observational methods, researchers have chosen reanalysis datasets as an alternative
63 for investigating LLJs. Reanalysis data have relatively better spatial and temporal coverage than rawinsonde
64 measurements, incorporate observations into the preliminary model simulations, provide more comprehensive
65 variables through assimilation, and contain broader domains. Rife et al. (2010) highlighted the global distribution of
66 identified nocturnal LLJs using reanalysis data with a horizontal grid spacing of 40 km, and even successfully
67 extracted some previously unknown jets, like Tarim nocturnal LLJ in northwest China, Ethiopia nocturnal LLJ, and
68 Namibia–Angola nocturnal LLJ. Doubler et al. (2015) applied the North American Regional Reanalysis (NARR)
69 dataset (~32 km) to generate long-term LLJ climatology in North America. Consistent with previous records,
70 Doubler's results supplemented the description of some smaller-scale LLJs. Similarly, Montini et al. (2019) compared
71 and validated the performance of five different reanalysis datasets in identifying LLJs. Their results showed the 38-
72 year climatology of South American LLJs with ERA-Interim data (~79 km).

73 Scientists have also conducted studies based on numerical simulations, which can more accurately represent LLJs than
74 reanalysis data sets, especially in the vertical direction, thereby yielding new insights into LLJs' features. Tang et al.
75 (2017) used an ensemble of dynamically downscaling regional climate simulations to generate the climatology of
76 Great Plains LLJ and predicted that the LLJ will occur more frequently during the nighttime in spring and summer in
77 mid-21st century. Jiménez-Sánchez et al. (2019) conducted a simulation for LLJs over the Orinoco River Basin by
78 dynamic downscaling of the Weather Research and Forecasting model (WRF). The simulation represented the jet

79 streaks better than previous studies within a broader region of wind enhancement and illustrated more detailed diurnal
80 evolution. Nevertheless, most general numerical simulations still represent the convective processes by the
81 parameterization scheme, which generates uncertainty in the results. These issues can be addressed by using
82 convection-permitting models with grid spacing under 5 km that adequately simulate the convections and other small-
83 scale processes (Liu et al., 2017, Li et al., 2019, Kurkute et al., 2020). Convection-permitting modeling describes the
84 underlying surface more accurately than coarse-resolution simulations and reanalysis data and shows ability in
85 investigations of LLJs near complex mountain areas. Du and Chen (2019) analyzed the LLJs over southern China by
86 using 4-km WRF model and revealed a solid relationship between the mesoscale lifting of LLJs and the convection's
87 initiation. They also highlighted the importance of coastal terrain. Overall, the finer-resolution tools tend to show more
88 comprehensive and precise results, offering detailed and accurate references to LLJs.

89 The formation mechanisms of LLJs have been studied extensively by researchers. In explaining the diurnal cycle
90 feature of the Great Plains LLJ, the inertial oscillation theory proposed by Blackadar (1957) and Stensrud (1996)
91 suggests that the LLJ is related to the friction change in the boundary layer. During the night, the jet-core wind is
92 enhanced after decoupling with near-surface friction. Holton (1967) and Parish (2000) developed the thermal wind
93 adjustment theory, which suggests that the horizontal pressure gradient changes because the atmosphere over sloping
94 terrain is warmer or because sea-land contrast influences the diurnal cycle of wind. Additionally, LLJs can also be
95 formed due to synoptic system forcing, as proposed by Uccellini et al. (1987) and Saulo et al. (2007). However,
96 convection-permitting models can help explain how LLJs form because they have precise descriptions of weather
97 systems and underlying orography. Using 4-km simulations, Fu et al. (2018) and Zhang et al. (2019) analyzed the
98 evolution of LLJs over mountainous areas in eastern and southwestern China, respectively. They concluded that
99 inertial oscillation plays a prominent role in and is responsible for the local precipitation peak at a certain time. Besides,
100 Shapiro et al. (2016) argued that the formation of some LLJs may not be impacted by a single factor and that a unified
101 theory analysis is thus required. Thus, a dataset that offers more information must be very popular. All these studies
102 have shown that convection-permitting models, with both finer coverage and resolutions, are a powerful tool for LLJ
103 characteristics research.

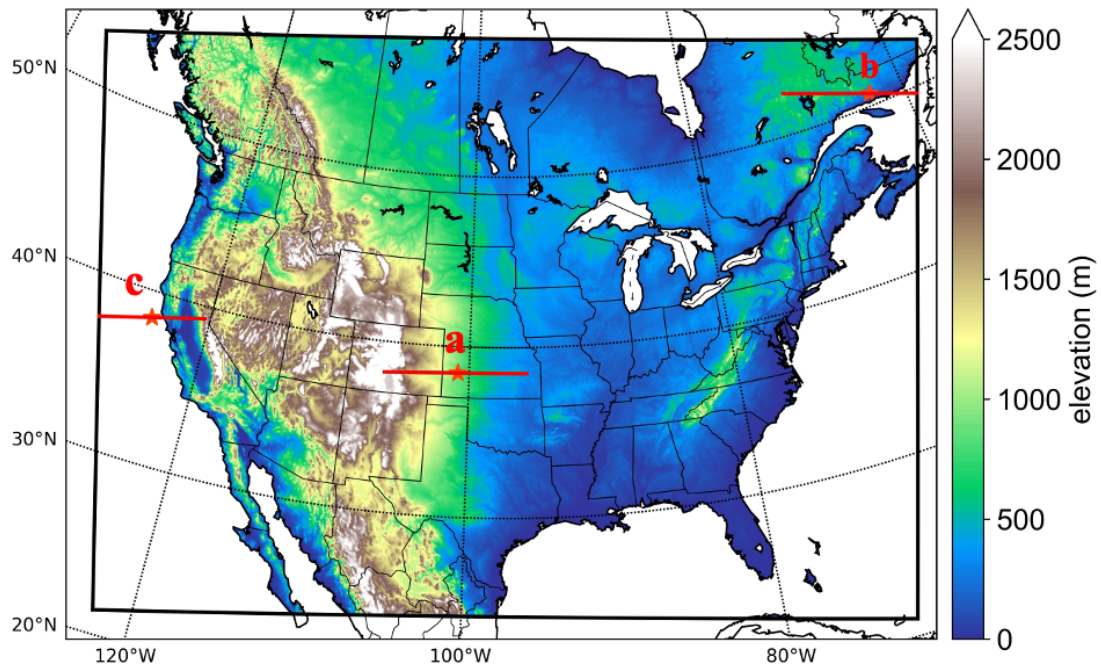
104 In this study, we utilize the 4-km convection-permitting WRF simulation (Liu et al., 2017) to analyze the features of
105 low-level jet systems across North America, improving the spatial and temporal resolutions. Section 2 introduces the

106 model configuration and the criteria for LLJ identification, Section 3 presents the characteristics of LLJ frequencies
107 in North America, and Section 4 illustrates the analysis of the background and mechanisms in several LLJ cases.
108 Finally, Section 5 provides the discussion and conclusion.

109 **2. Model configuration and methods**

110 **2.1 WRF setup**

111 This study utilized a convection-permitting Weather Research and Forecasting (WRF) dataset (Liu et al. 2017, Data
112 available at: <https://rda.ucar.edu/datasets/ds612.0/>) with a horizontal resolution of 4 km over North America, without
113 nesting. The domain covers the entire continental US, Southern Canada, and Northern Mexico, as illustrated in Figure
114 1. The simulation provides three-dimensional data at a temporal resolution of 3 hours, resulting in 8-time steps per
115 day. In the vertical direction, the data have 51 eta levels and can reach 50 hPa. It should be noted that there are five
116 layers under 500-m height and nine layers under 1 km are outputted above ground level, which means the WRF has a
117 better ability than other coarse modelling, to capture the LLJs occurring in the boundary layer. Considering the
118 computational cost for high-resolution modelling, this simulation period spans from 1st October 2000 to 30th
119 September 2013, and the six-hourly ERA-Interim reanalysis dataset of 0.7° resolution was used as input for the climate
120 simulation, the vertical layer depth of the forcing ERA-Interim data under 5 km is about 0.3-1.4 km (Hoffmann &
121 Spang, 2022). It is noted that 13 years is shorter than the normally defined climatology, but considering the
122 computational cost of high-resolution simulation, it is still a balanced compromise. This shorter period length was also
123 utilized to analyze the climate features of other weather events (Liu et al., 2017, Li et al., 2019). The simulation did
124 not apply any cumulus parameterization scheme due to the fine horizontal grid spacing, but other sub-grid scale
125 processes were parameterized by various physical schemes: the rapid radiative transfer model (RRTMG) (Iacono et
126 al., 2008) was used for simulating longwave and shortwave radiations, the Yonsei University (YSU) scheme was used
127 for representing the planetary boundary layer (Hong et al., 2006), and the Noah-MP model was used for computing
128 surface processes (Niu et al., 2011). In this study, the planetary boundary layer scheme is retained. Nonetheless, it
129 should be noted that this would introduce uncertainties to the simulation in the vertical direction, especially in regions
130 with complex topography.



131
 132 **Figure 1. Study domain of this convection-permitting model. The colors represent the elevation. The red lines and stars**
 133 **show the positions of investigated cross-section and jets in Section 4.**

134

135 **2.2 Methodology**

136 Using the threshold criteria proposed by Bonner (1968), this study identifies LLJs from the vertical wind profile of
 137 each grid point in the model output data. LLJs are present when the following conditions are met: (1) the height of the
 138 LLJ core maximum wind speed is below 3 km above the ground level (AGL); (2) the maximum wind speed is greater
 139 than or equal to 12 m s⁻¹; (3) from the height of the wind maxima to the height of the next minimum value or 3-km
 140 height (whichever is lower), the velocity of winds drop by at least 6 m s⁻¹; (4) the wind speed drops by at least 6 m s⁻¹
 141 below the level of wind maxima. Considering the importance of the meridional LLJ for heat and water vapor
 142 transport, this study addresses their frequencies in different meridional directions. According to Walter et al. (2008)
 143 and Doubler et al. (2015), the criteria for identifying different meridional LLJs are as follows: for southerly LLJs (S-
 144 LLJs), the jet-core wind direction is between 113° and 247°; for northerly LLJs (N-LLJs), the jet-core direction is
 145 between 293° and 67°. These criteria are used in this study.

146 Based on the identification criteria above, we determined if the LLJ existed at each grid point and consequently
 147 counted the occurrences of S-LLJs and N-LLJs. We also calculated the frequencies of LLJs in different seasons or

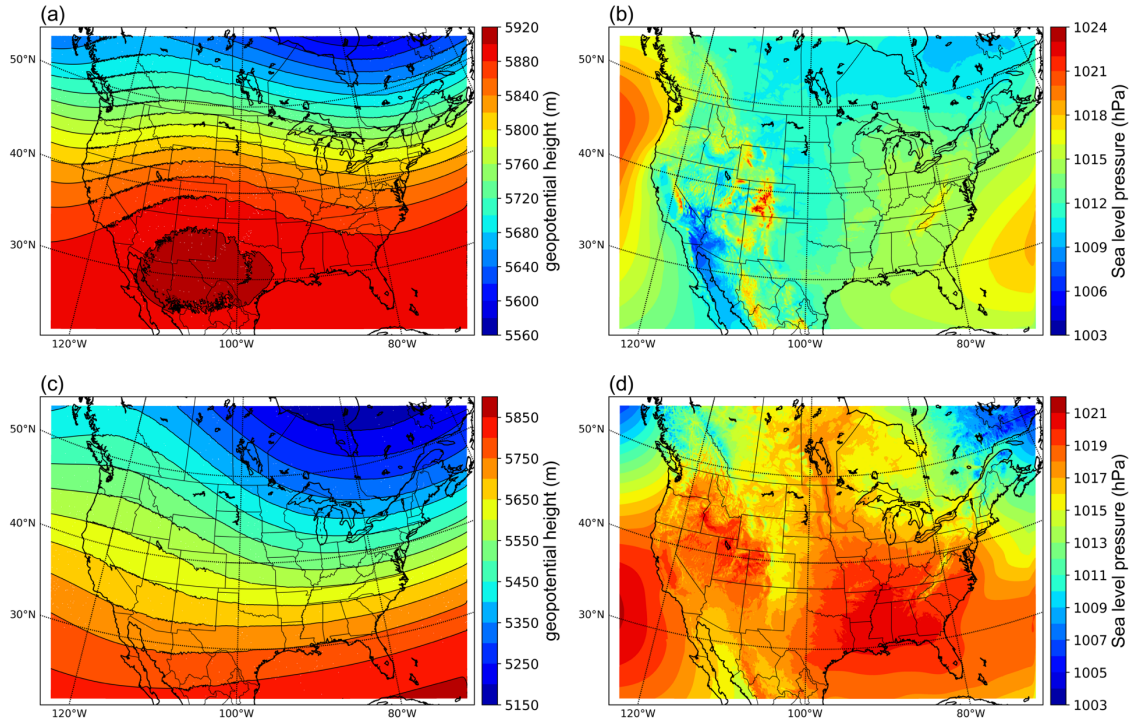
148 time steps. The frequency is defined as the percentage of the total number of occurrences for the selected accumulation
149 period. We generated the frequency distribution maps for LLJs in North America, which are illustrated in Section 3.

150 **3. The patterns of North American LLJs**

151 **3.1 Analysis of atmospheric circulation**

152 This study adopts model data to capture the climatological features of LLJs in North America. Considering the
153 relationship between LLJs and synoptical systems, we evaluated the ability of the convection-permitting model to
154 simulate the background atmospheric circulation. Figure 2 depicts the simulated multi-year analysis of geopotential
155 heights at 500 hPa and sea-level pressure isobars for summer and winter. In summer, at a height of 500 hPa (Figure
156 2a), In summer, the model depicts a trough in the east of the continental US, a ridge over the Rocky Mountains, and
157 the upper-air subtropical anticyclone crossing the southern US. At sea level (Figure 2b), the model captures the Azores
158 High-Pressure area in the Atlantic Ocean and the Hawaiian High-Pressure area in the Pacific.

159 In winter, the contours at the pressure value of 500 hPa (Figure 2c) show stronger fluctuating characteristics: the
160 eastern trough and western ridge over the continent strengthen, and the polar vortex extends to the northern US, while
161 most of North America is controlled by a cold high-pressure system. In addition, the subtropical anticyclone is too
162 weak to be found within the study domain. On the other hand, most of North America is controlled by a cold high-
163 pressure system at sea level (Figure 2d), and parts of the Icelandic Low and Aleutian Low appear on both east and
164 west of Canada, even though their centers are not captured in the domain. To summarize, the convection-permitting
165 model can simulate the features of semi-permanent centers of atmospheric circulations in North America, thus
166 demonstrating its strength in identifying the LLJs in this area.



167
 168 **Figure 2. Multi-year patterns of atmospheric circulations simulated by the convection-permitting model: (a) summer 500**
 169 **hPa geopotential height; (b) sea-level pressure in summer; (c)-(d) the same variables but in winter.**

170

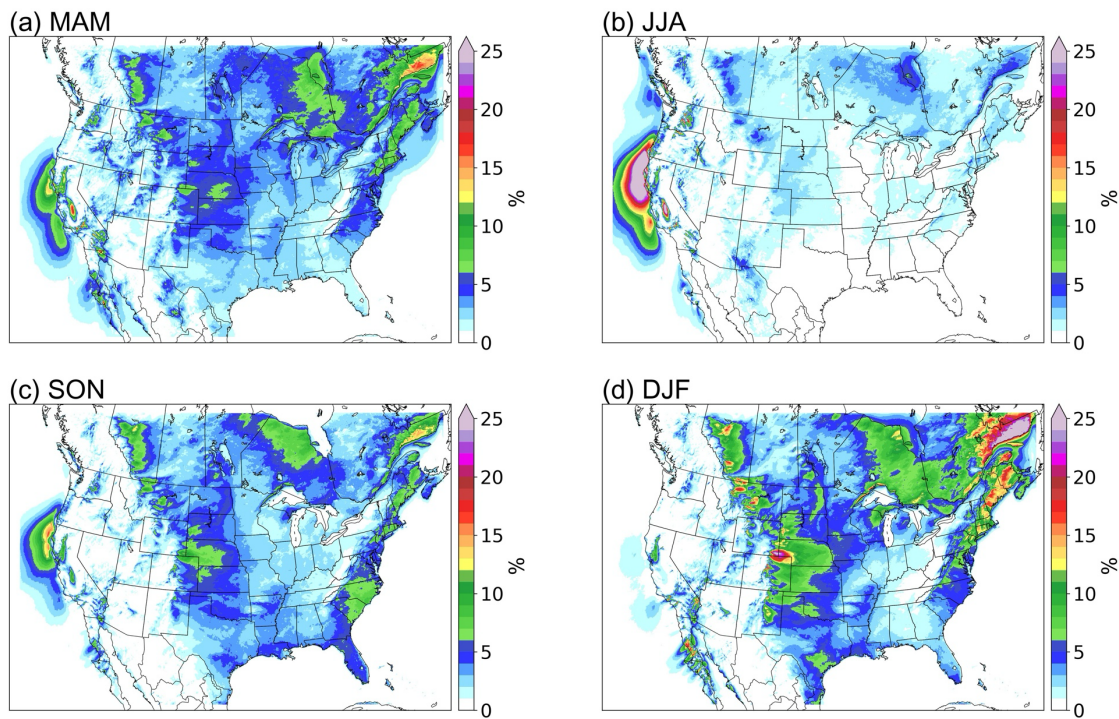
171 3.2 Seasonal variations of LLJs

172 3.2.1 Northerly LLJs

173 Figure 3 illustrates the seasonal frequency distribution of Northern Low-Level Jets (N-LLJs). The frequency is defined
 174 as the ratio of the total number of LLJ occurrences to the total number of time steps in each season. Notably, the
 175 California coastal LLJ peaks during the summer months (June, July, and August (JJA)), where frequencies exceed 25%
 176 over a broad area stretching from the southern Oregon coast to central California. In these regions, frequencies above
 177 5% can even extend into the Pacific Ocean near northern Baja California. However, transitioning from summer to
 178 autumn (September, October, and November (SON)), there is a sharp decline in the frequency of this LLJ, dropping
 179 to only 5%-15% within the core region, predominantly along the northern California coast. In winter (December,
 180 January, and February (DJF)), occurrences are sparse, at approximately 1%-2%.

181 Conversely, various N-LLJ phenomena are more prevalent during the colder seasons. These jets primarily occur near
 182 the eastern slopes of significant terrains such as the Rocky Mountains, Appalachian Mountains, and the Quebec

183 Labrador Plateau. High frequencies ($>10\%$) are observed from western Alberta to Oklahoma during winter, with hot
184 spots sporadically located in Alberta, Montana, Wyoming, and Colorado, where frequencies reach about 20%,
185 particularly between Colorado and Wyoming. In more than 25% of the wind profiles analyzed, N-LLJs were
186 identifiable. Along the Eastern US coast, N-LLJs predominantly stretch from Maine to South Carolina with peak
187 frequencies of approximately 15%-20%. In eastern Quebec, N-LLJs are most frequent in winter, exceeding 25%. The
188 simulation also detects the presence of N-LLJ in about 10% of the time steps over Hudson Bay. Notably, the
189 frequencies of all aforementioned N-LLJs significantly diminish in spring, becoming scarcely detectable in summer
190 with frequencies mostly under 5%.



191
192 **Figure 3. Seasonal occurrence frequency of N-LLJs. Frequency shown here is calculated by counting the number of**
193 **occurrences of LLJs in each three-hourly time step and then dividing the total number of LLJs in each season by the number**
194 **of time steps in that season.**

195 3.2.2 Southerly LLJs

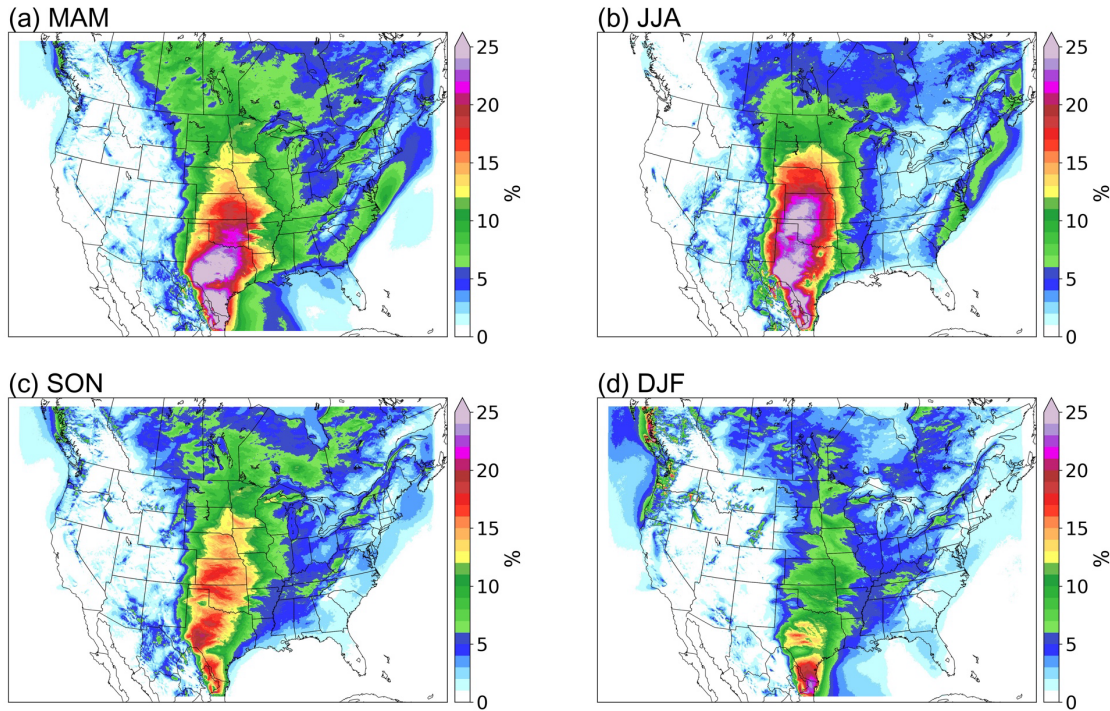
196 As to the patterns of S-LLJs in different seasons (see Figure 4), during winter, frequencies exceeding 10% are observed
197 across a vast area spanning from south Texas and the western Gulf of Mexico to southern Iowa, depicted as a deep
198 green area in Figure 4d. The greatest frequencies of S-LLJs ($>20\%$) are found along the border between northeastern

199 Mexico and the United States. In addition, about 15% of the simulated wind profiles in south-central Texas are
200 identified as S-LLJs (red clusters). In the spring (March, April, and May), the frequency expands significantly in >10%
201 of areas, with clear S-LLJ distributions detected in Manitoba, Saskatchewan, and other parts of Canada. The highest
202 frequencies are still found in the Texas-Mexico area, where the magnitude of these frequencies increases to over 25%.
203 This region (colored purple) also extends northward to occupy most of Texas. In winter, S-LLJs with occurrence
204 frequencies of above 15% extend to near Colorado and Nebraska.

205 By summer, the area with frequencies greater than 10% no longer reaches to the central Canadian prairie provinces.
206 The S-LLJs over the western Gulf of Mexico become nearly indiscernible in modeled data, with frequencies
207 approaching 0%. Conversely, the area with frequencies exceeding 25% expands northward and is segmented into three
208 distinct parts: along the northeast Mexico-Texas border, west-central Texas, and the central US Great Plains (western
209 Oklahoma and southern Kansas). Regions where over 15% of wind profiles are identified as S-LLJs also spread from
210 Colorado to near South Dakota.

211 In the fall, the magnitude of the frequency of S-LLJs decreases dramatically in the central US Plains and Texas. The
212 frequency still maintains a level greater than 15% in most areas, but with a maximum frequency of only 20% and
213 sporadically located in southwest Texas. The frequencies greater than 10% again expand northward and eastward in
214 this season, reaching Manitoba and Ontario.

215 Additionally, several smaller-scale S-LLJs are evident on the seasonal S-LLJ distribution map. In spring, a narrow
216 region of S-LLJs with a frequency greater than 5% along the eastern side of the Appalachians extends from Georgia
217 through the western Atlantic to southern Nova Scotia. Near eastern Maryland over the Atlantic, the frequency of S-
218 LLJs can exceed 10%. This narrow frequency belt persists through summer with the same coverage, though the
219 frequency magnitude diminishes, and the presence of frequencies greater than 10% is no longer visible. In winter, a
220 region where S-LLJ frequency exceeds 5% stretches from southwest Oregon to the west coast of British Columbia,
221 Canada. However, by spring, S-LLJs with frequencies above 5% occur solely over the ocean west of British Columbia,
222 and in summer, S-LLJs are virtually undetectable in this region.



223

224 **Figure 4. Seasonal frequency of S-LLJs.**

225 To summarize, for the LLJ systems that have been investigated by many researchers, the convection-permitting WRF
 226 model performs well in observing the Great Plains S-LLJ and California coastal N-LLJ during the summer. But as to
 227 the winter LLJs that lack attention, it is essential to compare and validate the occurrence and features revealed by
 228 WRF simulation. Therefore, the ERA5 reanalysis dataset is applied in this study for capturing the LLJs in winter using
 229 the same criterion. Appendix after the text shows the results of the comparison between ERA5 and WRF simulation.

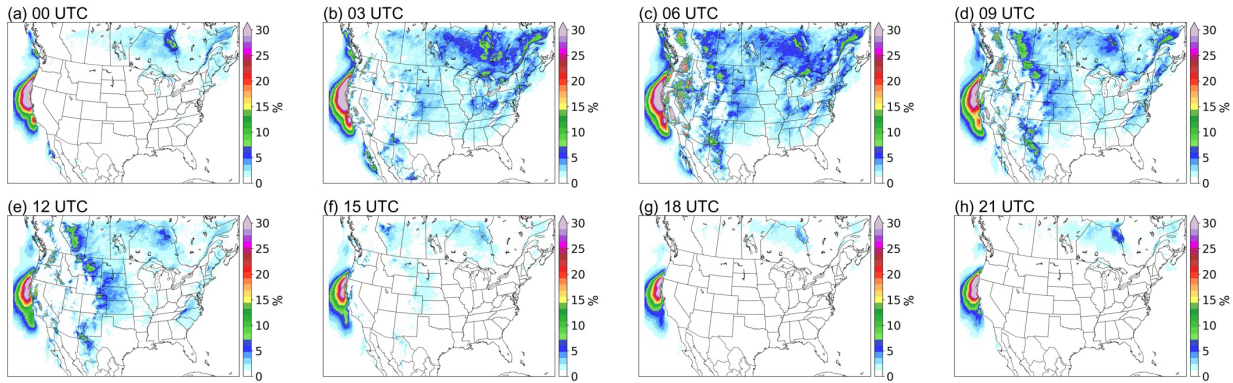
230 **3.3 Diurnal variations of LLJs**

231 To show the diurnal features of the LLJs, we selected summer and winter as the representative seasons because S-
 232 LLJs and N-LLJs occur most frequently in these seasons, respectively. Below, the descriptions are divided into N-
 233 LLJs and S-LLJs.

234 **3.3.1 Northerly LLJs**

235 The California coastal N-LLJ is the most highlighted low-level jet system in this region in summer. As seen in Figure
 236 5, it occurs throughout the day over the eastern Pacific Ocean from Oregon to the California coast. Figure 5 also shows
 237 that the California Coastal N-LLJ has diurnal characteristics: from 21 UTC (1 pm LST in California), the low-level

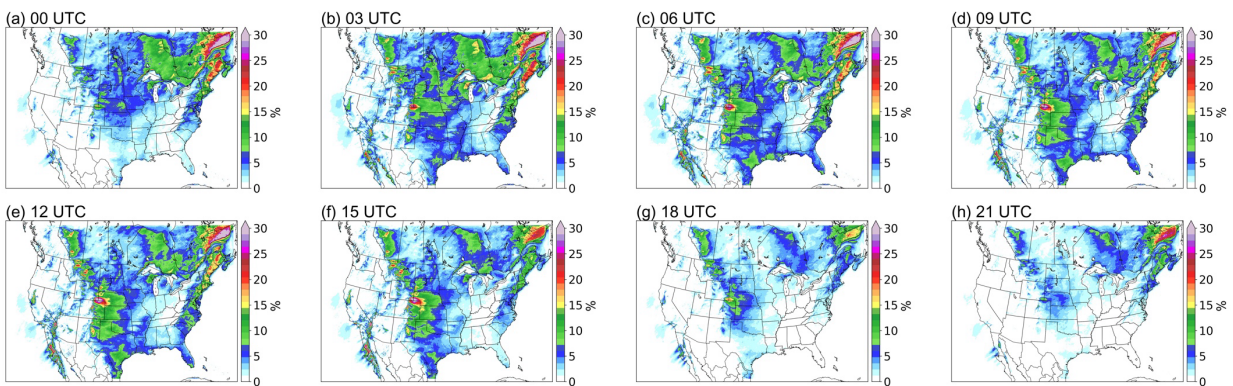
238 jet begins to develop, with a N-LLJ frequency of >30%, expanding until it reaches its maximum at 03 UTC – 06 UTC.
 239 Then the high-frequency coverage of the California coastal LLJ gradually shrinks, reaching the minimum at 18 UTC
 240 and only existing off the northwest coast of California.



241

242 **Figure 5. Diurnal frequency of N-LLJs in the summer (JJA).**

243 In winter (Figure 6), three types of N-LLJs over the Hudson Bay Lowlands, the eastern slopes of the Quebec Labrador
 244 Plateau, and the Appalachians display similar diurnal fluctuations. All three N-LLJs reach their highest frequency at
 245 03 UTC (10 pm EST) and their lowest at 18 UTC (1 pm EST). The only difference among the three types is that the
 246 smallest frequency of the Quebec N-LLJ still endures at a level of greater than 15%, while the other two N-LLJs
 247 mostly have frequencies of about 5%. The smallest frequency (~5%) of N-LLJs occurs downstream of the Rocky
 248 Mountains (over Alberta, Montana, and Kansas) at 21 UTC. In the subsequent development stage, the changes in the
 249 sporadic hot spots distributed near the eastern boundary of the Rocky Mountains are more significant. As seen in
 250 Figure 6, frequency starts growing from 00 UTC and then peaks at 12 UTC, especially the wind maxima located in
 251 Colorado, Wyoming, and Kansas, where the highest frequency can be >25%.

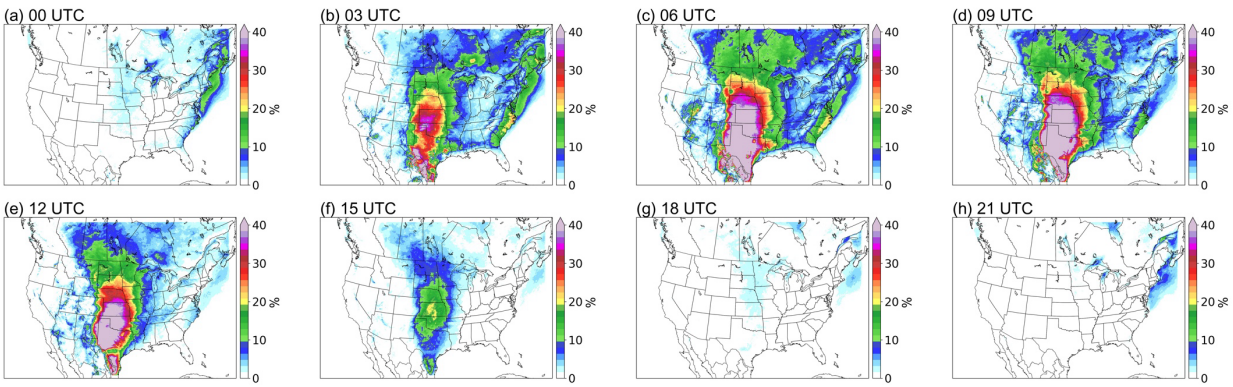


252

253 **Figure 6. Diurnal frequency of N-LLJs in winter (DJF).**

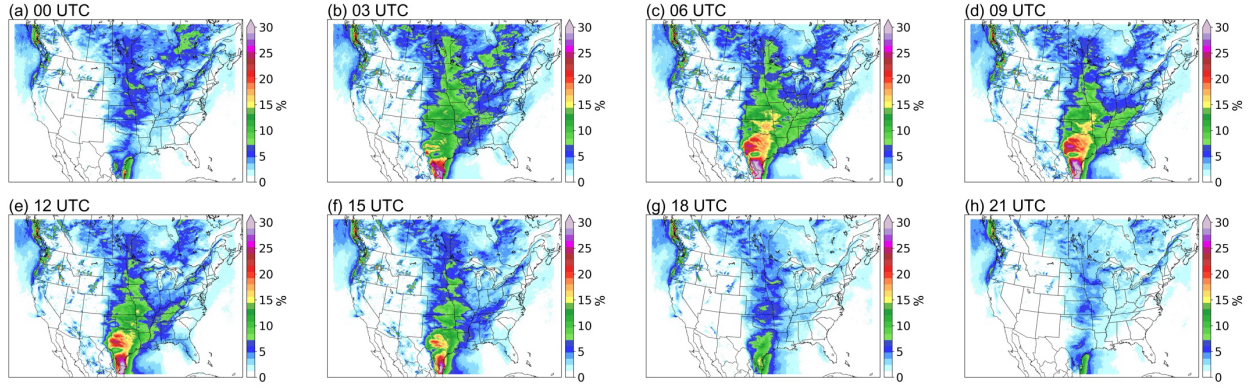
254 **3.3.2 Southerly LLJs**

255 In summer, the Great Plains S-LLJ occurs more frequently than in other seasons, and its diurnal variability is also the
256 strongest in this season (see Figure 7). At noon local time and in the afternoon (18 UTC – 00 UTC, 12-18 CST), almost
257 no S-LLJs occur over the central US (frequency <5% or about 0%). In contrast, the Great Plains LLJ begins to develop
258 at 03 UTC, when a frequency of over 25% extends from Mexico to Kansas. It reaches maximum strength at midnight
259 (06 UTC – 09 UTC, 00 – 03 CST), when the frequency reaches over 30% and the high-frequency coverage enlarges
260 to the Dakotas, the border of the eastern Rocky Mountains, and western Minnesota, Missouri, and Louisiana. Summer
261 S-LLJs are also active in southern Canada at night and in the early morning. In Saskatchewan, Manitoba, and central
262 Ontario (03 UTC – 12 UTC, as shown in Figure 7), S-LLJs are found with frequency >15%. In the eastern US and
263 Atlantic, S-LLJs occur most frequently at midnight (03 UTC – 06 UTC).



264
265 **Figure 7. Diurnal frequency of S-LLJs in summer (JJA).**

266 For the cold season (Figure 8), even though the Great Plains LLJ is the most inactive based on the description in
267 section 3.2, it still has a clear diurnal variation. Compared with the results in summer, the diurnal cycle of Great Plains
268 LLJ in winter is not that pronounced: It mainly occurs over the western Gulf of Mexico and southern Texas, with the
269 frequency in the afternoon (18 UTC – 21 UTC) declining to 5-10%. The S-LLJ develops from 03 UTC, gradually
270 generating two high-frequency (20%-25%) centers in mid- and southeastern Texas at 06 UTC – 12 UTC. As for the
271 S-LLJ near Vancouver Island, it is hard to see the diurnal variability: There is only a slight magnitude growth of
272 frequency from the afternoon (00 UTC) to the evening (06 UTC), and the coverage is almost the same.



273

274 **Figure 8. Diurnal frequency of S-LLJs in winter (DJF).**

275

276 **4 Formation and evolution mechanisms of various LLJs**

277 Section 3's results illustrate the occurrence frequency of LLJs over North America, particularly their seasonal and
 278 diurnal features. To explain the mechanisms, the inertial oscillation theory from Blackadar (1957) is used. Using this
 279 theory, we start from the horizontal momentum equations and divide the actual horizontal wind u/v into two
 280 components—geostrophic wind u_g/v_g and ageostrophic wind u_a/v_a :

281
$$\frac{d(u_g + u_a)}{dt} = -\frac{1}{\rho} \frac{\partial P}{\partial x} + f(v_g + v_a) \quad (1.1)$$

282
$$\frac{d(v_g + v_a)}{dt} = -\frac{1}{\rho} \frac{\partial P}{\partial y} - f(u_g + u_a) \quad (1.2)$$

283

284 In which ρ is air density, P is pressure, and f is the Coriolis parameter. Assuming the horizontal pressure gradient is

285 fixed, the geostrophic wind is a constant as well, which means $\frac{du_g}{dt} = \frac{dv_g}{dt} = 0$:

286
$$\frac{du_a}{dt} = -\frac{1}{\rho} \frac{\partial P}{\partial x} + f(v_g + v_a) \quad (2.2)$$

287
$$\frac{dv_a}{dt} = -\frac{1}{\rho} \frac{\partial P}{\partial y} - f(u_g + u_a) \quad (2.2)$$

288

289 When the definition of geostrophic wind $u_g = -\frac{1}{\rho f} \frac{\partial P}{\partial y}$ and $v_g = \frac{1}{\rho f} \frac{\partial P}{\partial x}$ is combined, the equation (2) is:

290
$$\frac{du_a}{dt} = f v_a \quad (3.1)$$

291
$$\frac{dv_a}{dt} = -f u_a \quad (3.2)$$

292

293 If $\frac{d}{dt}$ is taken to both sides of the equations (3), then we get $\frac{d^2 u_a}{dt^2} = -f^2 u_a$, and $\frac{d^2 v_a}{dt^2} = -f^2 v_a$, thereby:

294
$$u_a = c_1 \cos(ft) + c_2 \sin(ft) \quad (4.1)$$

295
$$v_a = c_2 \cos(ft) - c_1 \sin(ft) \quad (4.2)$$

296

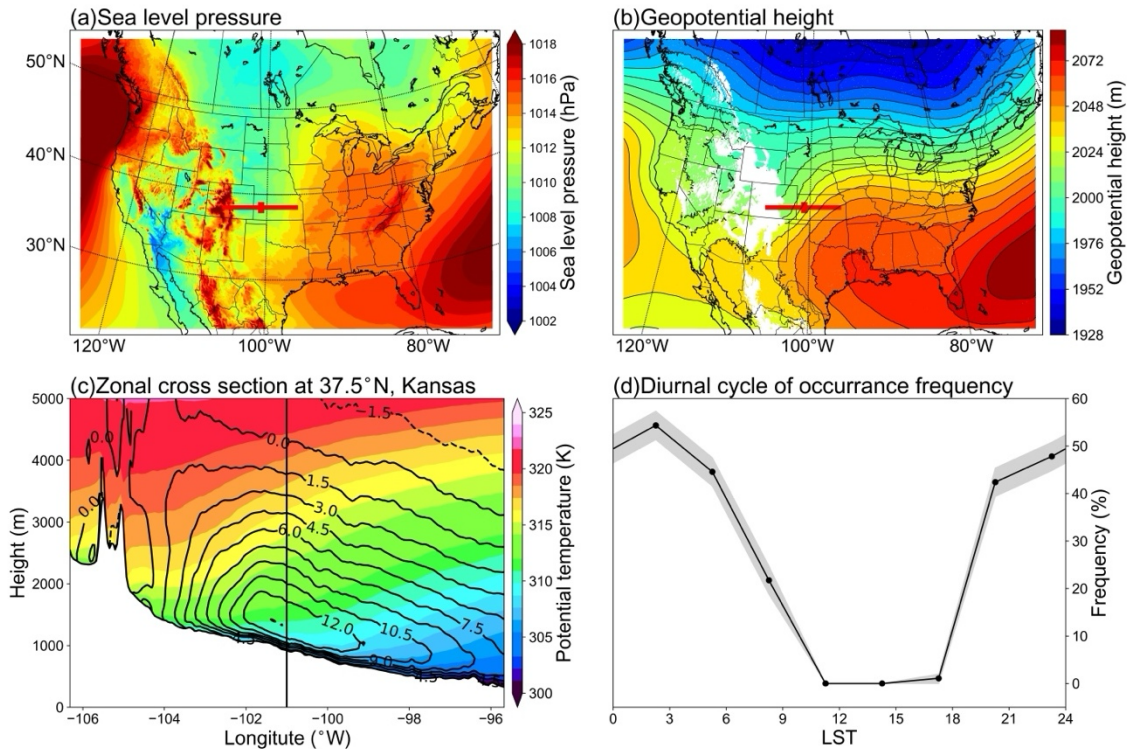
297 Therefore, according to the equations (4), the ageostrophic wind should theoretically have a circle-pattern variation
298 and the vector must rotate clockwise with a period of $2\pi/f$ (Blackadar, 1957; Van de Wiel et al., 2010). Under the
299 condition of a constant geostrophic wind—when the ageostrophic vector rotates from the opposite to the same
300 direction of geostrophic wind—the wind transitions from subgeostrophic to supergeostrophic. This change occurs
301 because of decoupling with surface friction effects, then the wind gets unbalanced.

302 Other theories also help explain the formation of LLJs, such as the sloping-terrain thermodynamic mechanism (Holton,
303 1967) and background synoptic system forcing (Uccellini et al., 1987). To understand the characteristics of the LLJs
304 in this study, three typical cases are analyzed: Great Plains S-LLJ, Quebec N-LLJ, and California coastal N-LLJ. The
305 locations for extracting data are shown in Figure 1 (solid lines and stars a, b, c).

306 **4.1 Great Plains S-LLJ**

307 As Section 3's results show (see Fig. 7), the Great Plains S-LLJ typically occurs in summer and more frequently at
308 night. To investigate its associated meteorological condition, this study extracts all the Great Plains S-LLJ cases occurs
309 at the jet core in JJA. The jet core is defined by where the mean meridional wind is the strongest on the cross-section,
310 and it locates at star A (shown in figure 1). The mean sea-level pressure and 800 hPa geopotential height are shown
311 in Figure 9a and 9b, respectively. The background large-scale circulations indicate that, at all the time points when
312 the Great Plains S-LLJ occurs, the range of the subtropical anticyclone extends east of the Great Plains at both ground
313 and low-level atmosphere. A high-pressure ridge is located near the gulf coast of Mexico and Texas (Figure 9b). Thus,
314 clearly, the zonal pressure/geopotential gradient in the central US guides the dominant southerly winds around this
315 region. The cross-section in Figure 9c illustrates a strong baroclinicity and shows that the isentropic line incline moves
316 from east to west, as is typical for the sloping-terrain heating effect (Holton, 1967). This effect generates an upslope
317 wind on the east side of the slope, and the airstream gradually turns northward due to the Coriolis force, creating the
318 southerly LLJs. On the other hand, as can be seen in the frequency cycle in Figure 9d, at noon local time (at the

319 selected point-a in Figure 1), the frequency of the Great Plains LLJ is very low (close to 0%), rising to more than 40%
 320 after 18 LST even if the radiation is not at the day's peak.



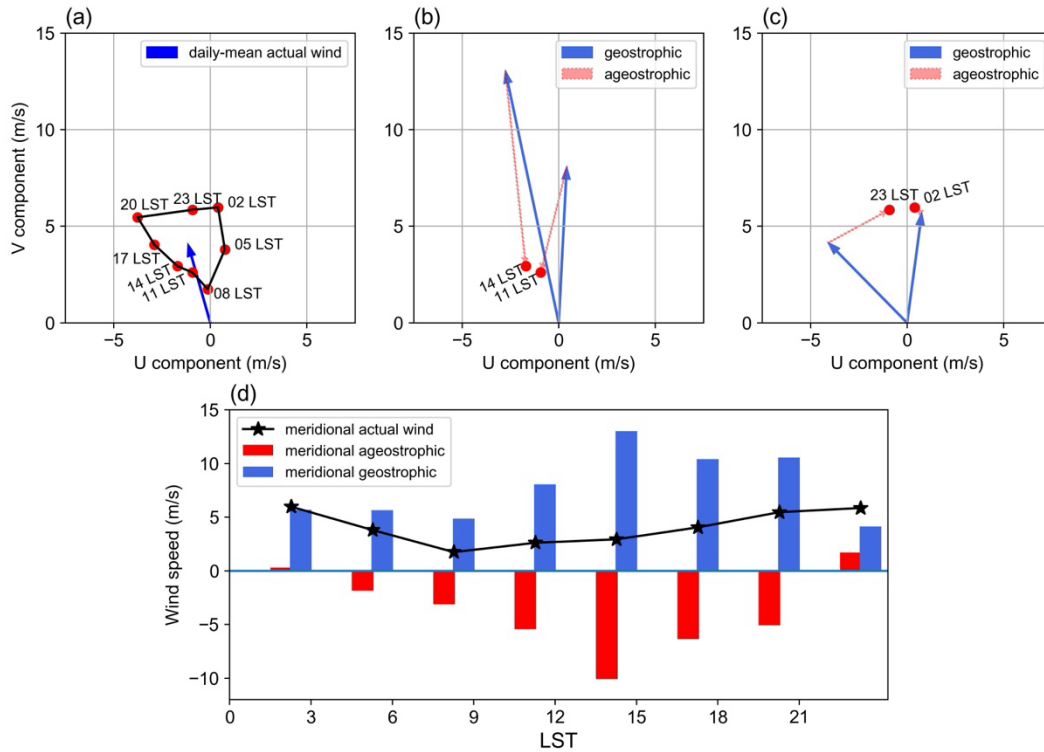
321
 322 **Figure 9. Background circulations of the Great Plains S-LLJ in JJA: (a) sea-level pressure, (b) geopotential height of 800**
 323 **hPa, (c) cross section including meridional winds (lines) and potential temperature (shading), and (d) diurnal cycle of**
 324 **frequency, with the shaded 95% confidence intervals. The red lines and points in (a) and (b) show the position of cross-**
 325 **section and chosen jet core, the vertical line in (c) shows the zonal location of the chosen jet core.**

326 To explain the nighttime enhancement of S-LLJ, we analyzed the wind vectors using inertial oscillation theory. To
 327 show more significant diurnal variation, all the time points, including the LLJs that did not occur, were considered.
 328 Figure 10a is the hodograph of jet-core winds at point-a near the Great Plains, and their temporal mean is computed
 329 at 3-hourly intervals in summer. It is noted here that the “jet-core” means the position where LLJ occurs horizontally
 330 the most frequently on the cross-section. Compared with the mean actual wind (blue arrow), the deviation at each
 331 local time shows a clear clockwise rotation. The wind speed begins increasing after 17 LST. Nevertheless, the analysis
 332 for Figure 9 indicates the sloping heating effect, meaning that the geostrophic wind is not fixed.

333 Thus, to obtain the ageostrophic winds, we computed the geostrophic components by pressure gradient and subtracted
 334 them from the actual airflow. According to the aforementioned definition of geostrophic wind, u_g and v_g are

335 calculated by the horizontal pressure gradient $\frac{\partial P}{\partial y}$ and $\frac{\partial P}{\partial x}$, respectively. By choosing four grids surrounding point-a, we
336 first interpolated the pressure value to the same level as the LLJ core height. Then, we adopted the central difference
337 equation $\frac{\Delta P}{\Delta x} = \frac{P_{i+1} - P_{i-1}}{x_{i+1} - x_{i-1}}$ or $\frac{\Delta P}{\Delta y} = \frac{P_{i+1} - P_{i-1}}{y_{i+1} - y_{i-1}}$ to obtain the pressure gradients at point-a, where i is the index of the grid
338 point at point-a.

339 Figures 10b and 10c display geostrophic wind vectors (blue arrows) and ageostrophic vectors (pink) at noon and
340 midnight. The southerly geostrophic flows are much stronger in the afternoon (10b) than at midnight. The ageostrophic
341 winds flow mostly in the opposite direction, limiting the actual wind speed. At night (10c), the geostrophic wind
342 direction rotates clockwise from that of the afternoon as the pressure gradient changes. Considering the relative
343 positions of blue and pink vectors at 23 LST and 01 LST, ageostrophic flow has rotated roughly 150 degrees to
344 enhance the geostrophic winds, thereby creating a super-geostrophic state. Although the inertial oscillation theory can
345 help explain some aspects of wind behavior, the real situation is more complex than initially thought. Figures 10b and
346 10c indicate that by 02 LST, the wind is almost entirely geostrophic with only negligible ageostrophic perturbations.
347 This suggests that the diurnal changes in the geostrophic wind and pressure gradient may provide a complicating
348 background that prevents the inertial oscillation theory from fully prevailing. While the inertial oscillation theory can
349 provide valuable insights, it should not be relied upon as the sole explanation for LLJs at the Great Plains. Instead, a
350 more comprehensive understanding of atmospheric dynamics is necessary to fully comprehend the behavior of the
351 wind, particularly when dealing with diurnally changing conditions. Figure 10d compares different meridional wind
352 components' amplitudes. The geostrophic wind contributes significantly to the southerly wind during the day, peaking
353 at 14 LST (blue bars). The northerly ageostrophic wind (red bars) is highest during the day, indicating the strongest
354 negative impact from friction. The meridional ageostrophic component decreases and eventually reverses at 23 LST,
355 showing a process from sub- to super-geostrophic status. In summary, the thermodynamic circulation near the slopes
356 of the Great Plains contributes to the strong southerly airflow, while the inertial oscillation plays a critical role in
357 forming the nocturnal southerly LLJ.



358

359 **Figure 10. (a) Hodograph of jet-core winds for the Great Plains S-LLJ every 3 hours over the whole JJA (red dots – solid**
 360 **line) and the daily averaged actual wind velocity (blue vector); vectors of mean jet-core geostrophic winds (solid blue) and**
 361 **ageostrophic winds (dashed red) at (b) 11/14 LST and (c) 23/02 LST; (d) diurnal cycles of meridional components of actual**
 362 **(black line), geostrophic (blue bars), and ageostrophic winds (red bars).**

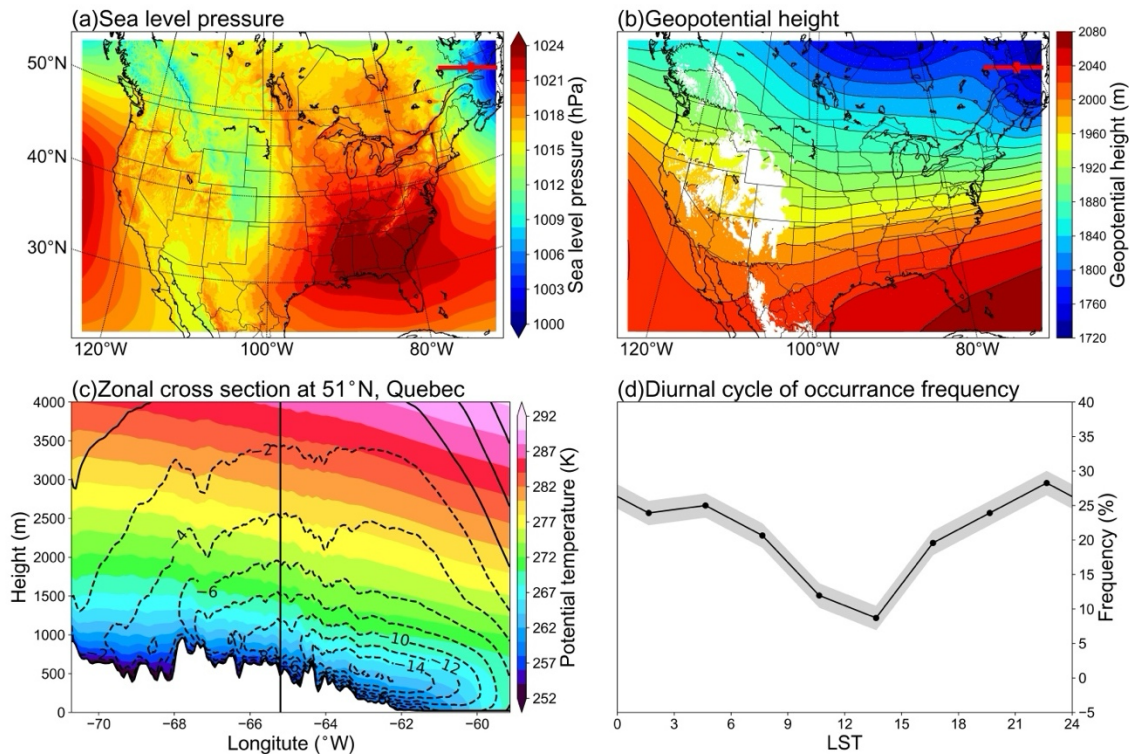
363

364 4.2 Quebec N-LLJ

365 Similarly, for the Quebec N-LLJ that is typically observed in winter, we selected all the LLJ cases at point-b (see the
 366 position in Figure 1) in DJF to generate the background circulation pattern. The background large-scale circulations
 367 indicate that the northeastern coast of Canada lies to the west of a strong surface low-pressure system (Figure 11a),
 368 while in the lower troposphere, a ridge on the east side of Hudson Bay occupies the Labrador Plateau (Figure 11b).
 369 This combination brings the northerly momentum to the downstream eastern coast. In fact, the background circulation
 370 is consistent with the shallow baroclinic structure of Quebec N-LLJ in winter, that is, the thermal difference between
 371 relatively warm sea and cold land. The cross-section in Figure 11c shows the thermodynamic structure of this N-LLJ:
 372 A well-defined low-level jet core is located above land and close to the coastline (approximately 63°W). With a
 373 maximum wind speed of more than 16 m s⁻¹ and a height of about 400 m, the jet core is located above the mixed layer

374 under the warm air covering and on the land side. Notably, the steep isentropic lines slope towards the ocean and
 375 finally sink at the position of 60°W. The onshore isentropic lines are flat and dense above the LLJ core, which means
 376 the environment is quite stable. This is helpful to maintain the structure of the LLJ, when vertical motion is inhibited,
 377 and horizontal wind is enhanced. Compared with the sloped isentropic lines in the Great Plain S-LLJ case (Figure 9c),
 378 the stability over Great Plain is not as high as in this case, so this difference in stability helps explain the variation in
 379 wind speeds between these two cases.

380 In addition, the diurnal cycle of frequency (Figure 11d) shows that the diurnal signal and peak frequency of Quebec
 381 N-LLJ are much weaker than the Great Plains S-LLJ, becoming weakest at noon and peaking at midnight, which is
 382 consistent with the results reported in Section 3. This diurnal variation can be explained by the baroclinicity near this
 383 region: At night in winter, the land temperature drops faster than the ocean temperature due to radiative cooling,
 384 enhancing the land-sea contrast and thereby the thermal wind above. The gentle slope on the east of the Labrador
 385 Plateau could generate the slope heating effect in the daytime. In this way, the related temperature gradient from east
 386 to west offsets the land-sea thermal difference.

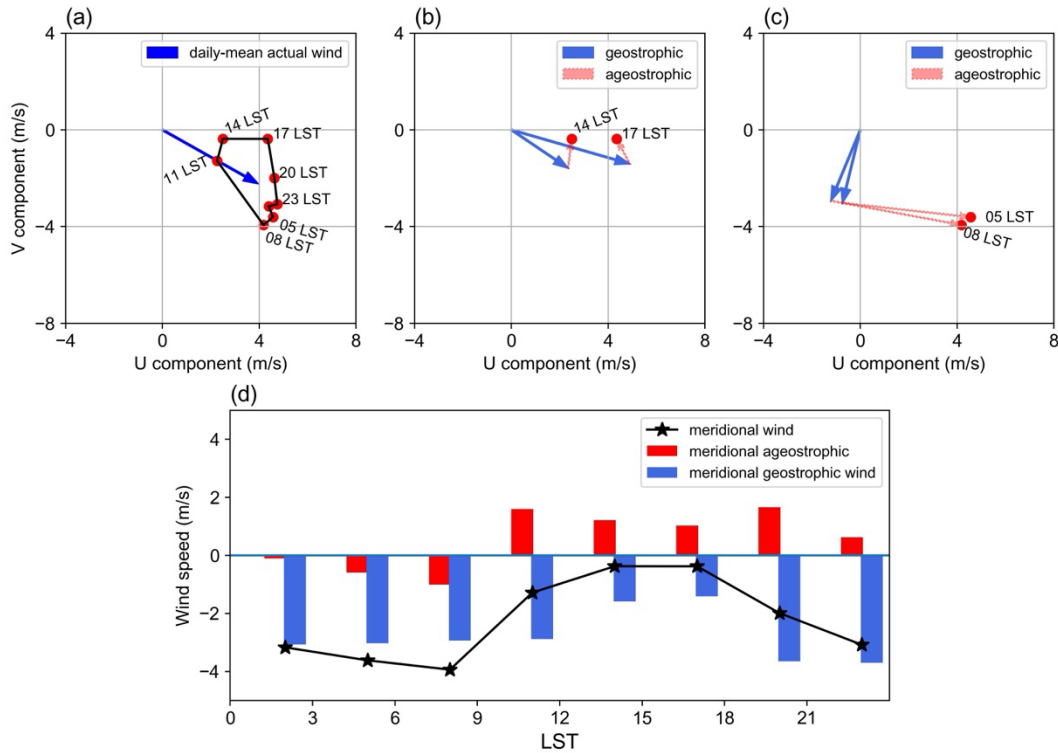


387
 388 **Figure 11. Background circulations of the Quebec N-LLJ in DJF: (a) sea-level pressure, (b) geopotential height of 800 hPa,**
 389 **(c) cross section including meridional winds (lines) and potential temperature (shading), and (d) diurnal cycle of frequency**

390 **with the shaded 95% confidence intervals. The red lines and points in (a) and (b) show the position of cross-section and**
391 **chosen jet core, the vertical line in (c) shows the zonal location of the chose jet core.**

392 As for the impact of inertial oscillation on the Quebec N-LLJ, the hodograph of averaged 3-hourly winds extracted at
393 point-b (Figure 12a) also illustrates a clear clockwise rotation of wind deviations compared with the daily mean (blue
394 arrow). Figure 12b and 12c show that the geostrophic and ageostrophic wind vectors contribute to the diurnal cycle in
395 the afternoon and morning, respectively. Even though the direction of geostrophic wind changes significantly, the
396 relative angles between ageostrophic and geostrophic arrows indicate that the ageostrophic flow rotates clockwise.
397 The geostrophic wind is weakened by ageostrophic wind in the afternoon (Figure 12b), whereas the supergeostrophic
398 state is generated in the morning (Figure 12c).

399 Focusing only on the meridional amplitudes validates this characteristic. In Figure 12d, the blue line that represents
400 the mean actual meridional wind has the same diurnal trend as the frequency variation in Figure 11d. The northerly
401 wind is weakest in the afternoon, peaking at night and in the early morning. Similarly, the variation of meridional
402 geostrophic flow has a consistent phase with the actual meridional wind, which is explained by the baroclinic structure
403 near the Quebec coast mentioned above. The meridional ageostrophic wind in this region also promotes the formation
404 of N-LLJ. The ageostrophic wind drags the geostrophic component in the afternoon, before reversing to a consistent
405 direction with the northerly geostrophic flow at night and in the morning. This trend is also the result of decreasing
406 friction after sunset. Therefore, the evolution of Quebec N-LLJ derives from both inertial oscillation and land-sea
407 thermal contrast in winter.



408

409 **Figure 12. (a) Hodograph of jet-core winds for the Quebec N-LLJ every 3 hours over the whole DJF (red dots – solid line)**
 410 **and the daily averaged actual wind velocity (blue vector); vectors of mean jet-core geostrophic winds (solid blue) and**
 411 **ageostrophic winds (dashed red) at (b) 14/17 LST and (c) 05/08 LST; (d) diurnal cycles of meridional components of actual**
 412 **(black line), geostrophic (blue bars), and ageostrophic winds (red bars).**

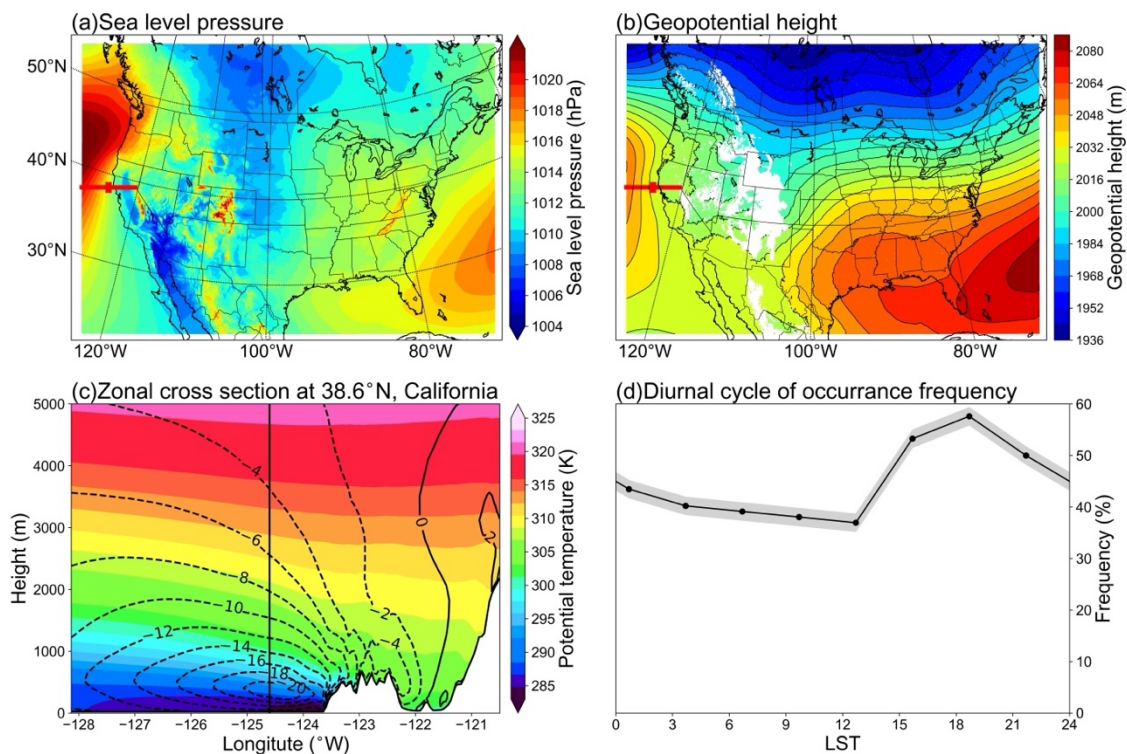
413

414 4.3 California coastal N-LLJ

415 The California coastal N-LLJ is similar to the one in Quebec, but it occurs more often in summer afternoons or
 416 evenings over the ocean. Figure 13a shows that a relatively strong high-pressure system is located on the east coast of
 417 the Pacific Ocean, trending NE-SW, although half of the structure is beyond the boundary of the domain. On the 800
 418 hPa isobaric surface in Figure 13b, there is also an anticyclone system in the same location, whose eastern contour is
 419 roughly parallel to the coastline, guiding the airflow to the south. Therefore, this pair is also forced by the thermal
 420 difference between land and sea, but contrary to the LLJ in Quebec, in summer, when the California LLJ occurs
 421 frequently, it has the characteristics of the cool sea-hot land. Figure 13b also shows that the isobars near Cape
 422 Mendocino are relatively strong, making the ridge of high pressure extend northeastward of the Cape. This extension
 423 is generally believed to occur due to pressure perturbation caused when northerly winds converge at this position after

424 being obstructed (Rahn and Parish, 2007). Regarding the cross-section structure shown in Figure 13c, the jet core is
 425 located at steep isentropic lines above the ocean at a height of 500 m. On the coast of California, the LLJ is close to
 426 the mountains. The maximum central wind speed of California coastal LLJ exceeds 20 m s⁻¹, whereas Quebec N-
 427 LLJ's max core wind is only about 14 m s⁻¹. Based on baroclinicity, the isentropic lines slope towards the continent
 428 and finally sink near the coastline.

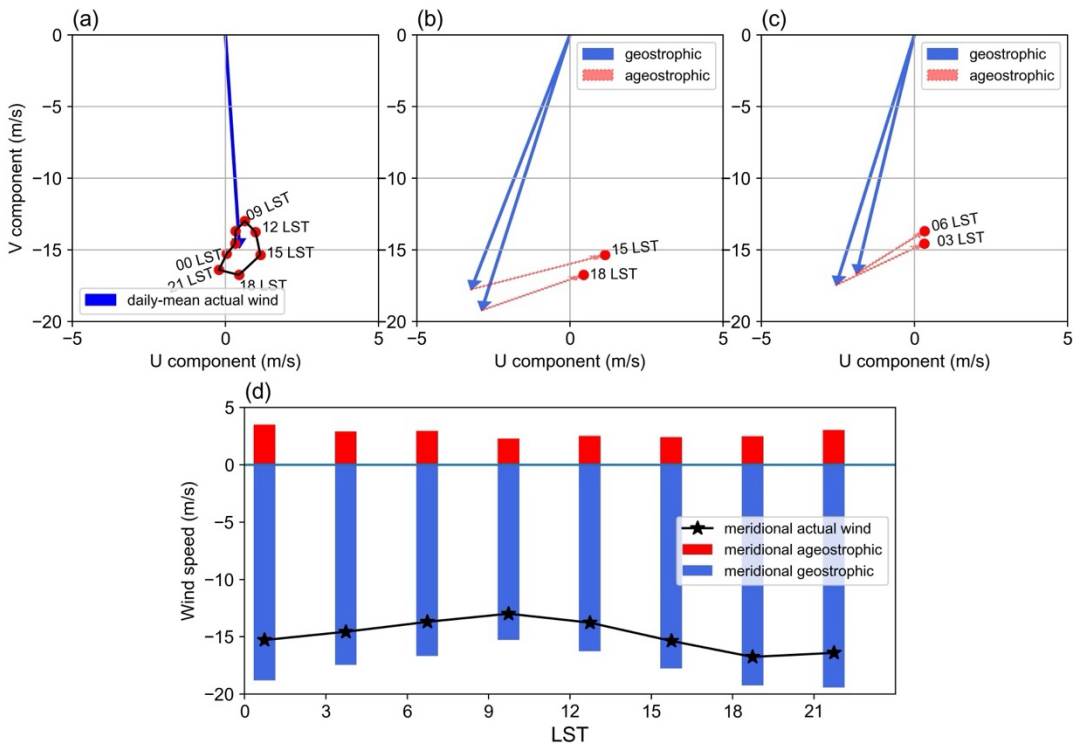
429 The core wind speed in California's coastal LLJ is higher than that of Quebec's LLJ because the land-sea contrast is
 430 more significant in summer than in winter and the formed sea breeze front generates flow convergence under the
 431 blockage caused by the west coast mountains. On the other hand, the atmosphere over the sea is more stable because
 432 the isentropic lines are flatter and denser than Quebec's case, which also favors the development of LLJ. In contrast,
 433 the east coast of Quebec is relatively gentle, which may account for its lower wind speed. California's LLJ occurs
 434 frequently at each time step, and its diurnal signal is weaker compared, for example, to the signal in the Great Plain
 435 S-LLJ. As well, the California signal stays at frequency of over 35%. California's LLJ occurs most frequently at
 436 around 18 LST and starts to decline after sunset, which is generally consistent with the coastal baroclinicity.



437
 438 **Figure 13. Background circulations of the California coastal N-LLJ in JJA: (a) sea-level pressure, (b) geopotential height**
 439 **of 800 hPa, (c) cross section including meridional winds (lines) and potential temperature (shading), and (d) diurnal cycle**

of frequency with the shaded 95% confidence intervals. The red lines and points in (a) and (b) show the position of cross-section and chosen jet core, the vertical line in (c) shows the zonal location of the chosen jet core.

The wind deviations for California’s N-LLJ shown in the hodograph (Figure 14a) still have a clockwise rotation in 24 hours. However, compared with the magnitude of the daily mean jet-core wind, this diurnal cycle is not quite as obvious as the cycle for Quebec and Great Plain LLJs, but it is similar to the frequency cycle shown in Figure 13d. In comparison between geostrophic and ageostrophic winds (Figure. 14b and 14c), during the afternoon (15 and 18 LST), the amplitude of geostrophic wind is the largest, and the ageostrophic flow diminishes the geostrophic wind. However, in the morning 12 hours later, the relative angle between ageostrophic and geostrophic vectors does not change, meaning that the ageostrophic wind is still weakening the geostrophic wind and that there is no rotation of the ageostrophic wind, as Blackadar inertial oscillation theory describes. Figure 14d helps to explain the change in meridional winds. Looking at the magnitudes of ageostrophic winds, one can see that all are weak and southerly and that they do not exhibit a significant diurnal signal. Furthermore, the change of geostrophic wind is highly consistent with the trend of the actual meridional wind. Thus, the N-LLJ in California can be considered mostly as geostrophic and the diurnal variation as being related to the change in geostrophic winds.



455

456 **Figure 14. (a) Hodograph of jet-core winds for the California coastal N-LLJ every 3 hours over the whole JJA (red dots –**
457 **solid line) and the daily averaged actual wind velocity (blue vector); vectors of mean jet-core geostrophic winds (solid blue)**
458 **and ageostrophic winds (dashed red) at (b) 15/18 LST and (c) 03/06 LST; (d) diurnal cycles of meridional components of**
459 **actual (black line), geostrophic (blue bars), and ageostrophic winds (red bars).**

460

461 **5 Discussion and conclusion**

462 This study applied a convection-permitting WRF model to conduct the analysis of LLJs in North America. The
463 previous research for LLJs mainly focused on observation data, which have no fine coverage in temporal or spatial
464 resolution. The studies using in-situ observations may ignore some important features. Despite their better coverage,
465 reanalysis datasets usually have a coarse spatial resolution, and can introduce large inaccuracies in the identification
466 of LLJs. In addition, the application of general numerical modeling cannot avoid the uncertainty caused by
467 parameterizing small-scale physical processes. In contrast, high-resolution convection-permitting climate simulations
468 can provide relatively more comprehensive descriptions of LLJs, especially for areas with complex geographic
469 conditions or regions that lack soundings. Previous studies using high-resolution models conducted case analyses only
470 of LLJs in a specific region (Aird et al., 2022). By expanding the target domain to the whole of North America and
471 revealing the climatological characteristics of LLJs in different regions and scales, this paper provides an accurate
472 reference for future research on LLJ-related processes in North America.

473 The convection-permitting WRF model is able to recapture some LLJs that have been previously studied, such as the
474 Great Plain S-LLJ and the California coastal N-LLJ in the eastern Pacific Ocean and has obtained relatively consistent
475 results. The results indicate that the S-LLJ in the central US Plain is the most frequent and active in warm seasons and
476 that three critical high-frequency centers occur in summer: the northeast Mexico-Texas border, west-central Texas,
477 and western Oklahoma to southern Kansas. This last result is consistent with the climatology generated by Doubler et
478 al. (2015) using the NARR reanalysis data, but the patterns here are more representative of the topographic features
479 in central and southern Texas. In addition, compared with the 40-year rawinsonde climatology in the central US by
480 Walters et al. (2008), our study reveals that the S-LLJ frequency range of these three centers in the central US in
481 summer is 25%-30%, which is slightly lower than the 35% reported in the 2008 study. However, given the
482 underestimated frequencies of 15%-20% in NARR climatology, there is an advantage of using high-resolution
483 simulations in the vertical direction. Even though the simulation period does not match the time range of the literature
484 exactly, the characteristics transcend specific time frames still offer a reference.

485 The convection-permitting simulation can also capture LLJs that were poorly detected previously using coarser
486 resolution models and observational datasets. The winter N-LLJs over the eastern Rocky Mountains described in this
487 paper are generally distributed over the central US from the Dakotas to Oklahoma with a low frequency (>10%) and
488 over several sporadic small areas with a high frequency (>20%) along the boundary of the Rockies. The main
489 seasonal/diurnal variations identified in this study agree with those seen using rawinsonde data (Walters et al., 2008)
490 and NARR reanalysis (Douber et al., 2015). But the frequency of the LLJ occurrence over Nebraska-Kansas was
491 underestimated in both convection-permitting simulations (~10%) and NARR (~7%), while high-frequency hot spots
492 from Alberta to Colorado were not detected in either of the above-mentioned studies, probably because measurements
493 are lacking in these regions. The high-resolution simulation also detected LLJs on which researchers have hardly
494 focused: N-LLJs near the eastern Quebec coast and in the Appalachians Mountains, as well as an S-LLJ over the
495 British Columbia coast. In the work of Douber et al. (2015), these LLJs were shown in the climatology patterns, but
496 the 4-km WRF simulation offered more detailed descriptions of their locations. For example, this study found that the
497 Appalachian N-LLJ extends from Georgia to the northwestern Atlantic, especially on summer nights (03 UTC – 06
498 UTC), while NARR only captured LLJ occurrences over the middle coast of the Atlantic. The maximum frequency
499 (7-10%) detected in the NARR study is also less than what is illustrated here. As for the Quebec N-LLJ, the 4-km
500 WRF revealed that it mostly occurs onshore near the coast with a frequency of over 25% in winter, but NARR only
501 provided a coarse occurrence distribution over northeastern Canada.

502 Based on the inertial oscillation theory (Blackadar, 1957) and the baroclinic theory near complex terrain (Holton,
503 1967), this paper also analyzed the background and formation mechanisms of three LLJs: the Great Plain S-LLJ,
504 Quebec N-LLJ, and California coastal N-LLJ. Generally, all these LLJs are impacted by the thermodynamic
505 circulations generated near their topography. The Great Plain S-LLJ is affected by slope heating, and the LLJs over
506 Quebec and California are associated with the sea-land contrast. When the geostrophic and ageostrophic components
507 of the LLJs are compared, results show that the inertial oscillation better explains the night enhancement of the Great
508 Plains S-LLJ and that the diurnal feature of the Quebec N-LLJ is influenced by the combination of the Holton and
509 Blackadar theories. As for the California coastal N-LLJ, no supergeostrophic state is found, making coastal
510 baroclinicity variation a dominant factor for this LLJ's evolution the geostrophic wind changes.

511 This research adds to the existing knowledge of characteristics of the low-level wind maxima in North America, thus
512 helping researchers obtain more reliable references about LLJs in this domain. Meanwhile, with the high-resolution
513 features, it can provide more robust explanations for other interdisciplinary fields. The research also advances
514 knowledge about the formation of three dominant LLJs. Although the 13-year simulation is likely too short to provide
515 an ideal long-term climatic analysis, it is a less expensive option for finer numerical modelling in large domains.
516 Additionally, we acknowledge certain limitations in the convection-permitting WRF simulation. While the vertical
517 resolution in the boundary layer of this simulation is enhanced compared to other RCMs or reanalysis datasets, it
518 remains inferior to the observation density of radiosonde soundings. Consequently, the underestimation of LLJ events
519 in this paper is expected, as noted in previous comparative analyses. Furthermore, numerical models inherently possess
520 biases and uncertainties. Although employing the convection-permitting scale mitigates some of these uncertainties,
521 it is important to recognize these limitations in referring to the results. But it is also believed that with the advancement
522 of technology, there will be longer and more accurate high-resolution simulations in the future. Future work will
523 address the features and formation mechanisms of the small-scale low-level wind maxima that have yet to be
524 investigated.

525 **Acknowledgments**

526 All authors thank the support of the Global Water Futures Program by the Canada First Research Excellence and the
527 NSERC Discovery Grant.

528

529 **Data Availability Statement**

530 The WRF simulation over CONUS can be accessed at Research Data Archive of NCAR
531 <https://rda.ucar.edu/datasets/ds612.0/>.

532

533 **Author contribution**

534 Xiao Ma: Conceptualization; data curation; formal analysis; investigation; methodology; visualization; writing-
535 original draft.

536 Yanping Li: Conceptualization; funding acquisition; investigation; methodology; project administration; supervision;
537 validation; writing-review and editing.

538 Zhenhua Li: Data curation; methodology; validation; visualization; writing-review and editing.

539 Fei Huo: Data curation; methodology; validation; visualization; writing-review and editing.

540

541 **Competing interests**

542 All authors disclosed no relevant relationships.

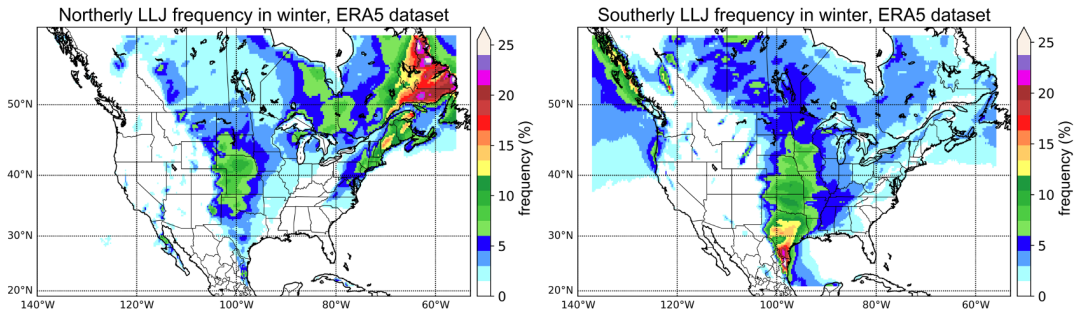
543

544 **Appendix**

545 **Winter LLJs captured by ERA5 Dataset**

546 The convection-permitting WRF simulation exhibited excellent performance in investigating well-known LLJ systems,
547 such as the California coastal N-LLJ and the Great Plains S-LLJ. Moreover, this appendix validates WRF-simulated
548 significant winter jet systems over North America using the ERA5 reanalysis dataset. ERA5 is a global atmospheric
549 reanalysis dataset produced by the European Centre for Medium-Range Weather Forecasts (ECMWF). It provides
550 hourly data on a horizontal grid space of approximately 31 km, and the time range covers from 1979 till the present.
551 ERA5 data is widely used in climate research, weather forecasting, and various applications that require high-quality
552 atmospheric data.

553 The validation period is the same as the WRF simulation (2000-2013). From the Figure A1 below, it is evident that
554 during winter, a greater number of significant N-LLJ systems in the North American continent are mostly concentrated
555 in eastern Canada. In most parts of Newfoundland and southeastern Quebec, the occurrence frequency of N-LLJs
556 exceeds 15%, and the maximum can even surpass 25%. However, in the WRF simulation (Figure 3d), the model can
557 only capture N-LLJs on the north bank of the St. Lawrence River due to the northern boundary of the study domain
558 overlapping with the Quebec border. In comparison, the WRF-simulated frequency of N-LLJs in southeastern Quebec
559 essentially exceeds 25%, overestimated by about 5% compared to the ERA5 reanalysis. Additionally, it is worth noting
560 that the N-LLJs along the downstream of Rockies are also identified in the ERA5 dataset. The areas where the
561 frequency exceeds 5% are mainly distributed from Alberta to northern Texas, consistent with the findings in Section
562 3.2.1. Moreover, the high-value center ($>10\%$) is located in central Kansas. In terms of the differences between the
563 two datasets, the results of the WRF simulation match more geographical features and reveal scattered high-value
564 spots ($>15\%$) in some regions with special terrains (see Figure 3d). Furthermore, the winter Great Plains S-LLJs in
565 ERA5 reanalysis exhibit similar features, with frequencies ranging from around 15% to 20% in southern Texas. In
566 summary, the WRF model can accurately capture the features of winter LLJ systems, which are validated by the ERA5
567 reanalysis dataset over northern America. Even though the frequency of LLJs occurrence is overestimated, the
568 convection-permitting WRF simulation can provide detailed descriptions of LLJs near complex terrains.



569

570 **Figure A1. Winter occurrence frequency of N-LLJs (left) and S-LLJs (right).**

571

572

573

574 **Data Availability Statement**

575 The ERA5 dataset is available on the Copernicus Climate Change Service Information website.

576 <https://cds.climate.copernicus.eu/#!/home>

577

578

579 **References**

- 580 Aird, J. A., Barthelmie, R. J., Shepherd, T. J. and Pryor, S. C.: Occurrence of Low-Level Jets over the Eastern U.S.
581 Coastal Zone at Heights Relevant to Wind Energy, *Energies*, 15(2), 445, doi:10.3390/en15020445, 2022.
- 582 Blackadar, A. K.: Boundary Layer Wind Maxima and Their Significance for the Growth of Nocturnal Inversions,
583 *Bulletin of the American Meteorological Society*, 38(5), 283–290, doi:10.1175/1520-0477-38.5.283, 1957.
- 584 Bonner, W. D.: CLIMATOLOGY OF THE LOW LEVEL JET, *Monthly Weather Review*, 96(12), 833–850,
585 doi:10.1175/1520-0493(1968)096<0833:cotllj>2.0.co;2, 1968.
- 586 Chen, G. T.-J., Wang, C.-C. and Lin, D. T.-W.: Characteristics of Low-Level Jets over Northern Taiwan in Mei-Yu
587 Season and Their Relationship to Heavy Rain Events, *Monthly Weather Review*, 133(1), 20–43, doi:10.1175/mwr-
588 2813.1, 2005.
- 589 Doubler, D. L., Winkler, J. A., Bian, X., Walters, C. K. and Zhong, S.: An NARR-Derived Climatology of Southerly
590 and Northerly Low-Level Jets over North America and Coastal Environs, *Journal of Applied Meteorology and*
591 *Climatology*, 54(7), 1596–1619, doi:10.1175/jamc-d-14-0311.1, 2015.
- 592 Du, Y. and Chen, G.: Heavy Rainfall Associated with Double Low-Level Jets over Southern China. Part II: Convection
593 Initiation, *Monthly Weather Review*, 147(2), 543–565, doi:10.1175/mwr-d-18-0102.1, 2019.
- 594 Frisch, A. S., Orr, B. W. and Martner, B. E.: Doppler Radar Observations of the Development of a Boundary-Layer
595 Nocturnal Jet, *Monthly Weather Review*, 120(1), 3–16, doi:10.1175/1520-
596 0493(1992)120<0003:drootd>2.0.co;2, 1992.
- 597 Fu, P., Zhu, K., Zhao, K., Zhou, B. and Xue, M.: Role of the nocturnal low-level jet in the formation of the morning
598 precipitation peak over the Dabie Mountains, *Advances in Atmospheric Sciences*, 36(1), 15–28, doi:10.1007/s00376-
599 018-8095-5, 2018.
- 600 Gadde, S. N. and Stevens, R. J. A. M.: Effect of low-level jet height on wind farm performance, *Journal of Renewable*
601 *and Sustainable Energy*, 13(1), 013305, doi:10.1063/5.0026232, 2021.

602 Hodges, D. and Pu, Z.: Characteristics and Variations of Low-Level Jets and Environmental Factors Associated with
603 Summer Precipitation Extremes over the Great Plains, *Journal of Climate*, 32(16), 5123–5144, doi:10.1175/jcli-d-18-
604 0553.1, 2019.

605 Hoffmann, L. and Spang, R.: An assessment of tropopause characteristics of the ERA5 and era-interim meteorological
606 reanalyses, *Atmospheric Chemistry and Physics*, 22(6), 4019–4046, doi:10.5194/acp-22-4019-2022, 2022.

607 Holton, J. R.: The diurnal boundary layer wind oscillation above sloping terrain, *Tellus*, 19(2), 199–205,
608 doi:10.1111/j.2153-3490.1967.tb01473.x, 1967.

609 Hong, S.-Y., Noh, Y. and Dudhia, J.: A New Vertical Diffusion Package with an Explicit Treatment of Entrainment
610 Processes, *Monthly Weather Review*, 134(9), 2318–2341, doi:10.1175/mwr3199.1, 2006.

611 Hu, X.-M., Klein, P. M., Xue, M., Lundquist, J. K., Zhang, F. and Qi, Y.: Impact of Low-Level Jets on the Nocturnal
612 Urban Heat Island Intensity in Oklahoma City, *Journal of Applied Meteorology and Climatology*, 52(8), 1779–1802,
613 doi:10.1175/jamc-d-12-0256.1, 2013.

614 Iacono, M. J., Delamere, J. S., Mlawer, E. J., Shephard, M. W., Clough, S. A. and Collins, W. D.: Radiative forcing
615 by long-lived greenhouse gases: Calculations with the AER radiative transfer models, *Journal of Geophysical*
616 *Research*, 113(D13), doi:10.1029/2008jd009944, 2008.

617 Jain, P. and Flannigan, M.: The relationship between the Polar Jet Stream and extreme wildfire events in North
618 America, *Journal of Climate*, 1–59, doi:10.1175/jcli-d-20-0863.1, 2021.

619 Jiménez-Sánchez, G., Markowski, P. M., Jewtoukoff, V., Young, G. S. and Stensrud, D. J.: The Orinoco Low-Level
620 Jet: An Investigation of Its Characteristics and Evolution Using the WRF Model, *Journal of Geophysical Research:*
621 *Atmospheres*, 124(20), 10696–10711, doi:10.1029/2019jd030934, 2019.

622 Kurkute, S., Li, Z., Li, Y. and Huo, F.: Assessment and projection of the water budget over Western Canada using
623 convection-permitting weather research and forecasting simulations, *Hydrology and Earth System Sciences*, 24(7),
624 3677–3697, doi:10.5194/hess-24-3677-2020, 2020.

625 Li, Y., Li, Z., Zhang, Z., Chen, L., Kurkute, S., Scaff, L. and Pan, X.: High-resolution regional climate modeling and
626 projection over Western Canada using a weather research forecasting model with a pseudo-global warming approach,
627 *Hydrology and Earth System Sciences*, 23(11), 4635–4659, doi:10.5194/hess-23-4635-2019, 2019.

628 Lin, Y., Wang, C., Yan, J., Li, J. and He, S.: Observation and simulation of low-level jet impacts on 3D urban heat
629 islands in Beijing: A case study, *Journal of the Atmospheric Sciences*, 79(8), 2059–2073, doi:10.1175/jas-d-21-0245.1,
630 2022.

631 Liu, C., Ikeda, K., Rasmussen, R., Barlage, M., Newman, A. J., Prein, A. F., Chen, F., Chen, L., Clark, M., Dai, A.,
632 Dudhia, J., Eidhammer, T., Gochis, D., Gutmann, E., Kurkute, S., Li, Y., Thompson, G. and Yates, D.: Continental-
633 scale convection-permitting modeling of the current and future climate of North America, *Climate Dynamics*, 49(1–
634 2), 71–95, doi:10.1007/s00382-016-3327-9, 2016.

635 Ma, X., Li, Y. and Li, Z.: The projection of Canadian wind energy potential in future scenarios using a convection-
636 permitting regional climate model, *Energy Reports*, 8, 7176–7187, doi:10.1016/j.egyr.2022.05.122, 2022.

637 Miao, Y., Guo, J., Liu, S., Wei, W., Zhang, G., Lin, Y., Zhai, P., Zhai, P., Lin, Y., Zhang, G., Wei, W., Liu, S., Guo,
638 J. and Miao, Y.: The Climatology of Low-Level Jet in Beijing and Guangzhou, China, *Journal of Geophysical*
639 *Research: Atmosphere*, 123(5), 2816–2830, doi:10.1002/2017jd027321, 2018.

640 Mitchell, M. J., Arritt, R. W. and Labas, K.: A Climatology of the Warm Season Great Plains Low-Level Jet Using
641 Wind Profiler Observations, *Weather and Forecasting*, 10(3), 576–591, doi:10.1175/1520-
642 0434(1995)010<0576:acotws>2.0.co;2, 1995.

643 Montini, T. L., Jones, C. and Carvalho, L. M. V.: The South American Low-Level Jet: A New Climatology, Variability,
644 and Changes, *Journal of Geophysical Research: Atmospheres*, 124(3), 1200–1218, doi:10.1029/2018jd029634, 2019.

645 Munday, C., Washington, R. and Hart, N.: African Low-Level Jets and Their Importance for Water Vapor Transport
646 and Rainfall, *Geophysical Research Letters*, 48(1), doi:10.1029/2020gl090999, 2021.

647 Niu, G.-Y., Yang, Z.-L., Mitchell, K. E., Chen, F., Ek, M. B., Barlage, M., Kumar, A., Manning, K., Niyogi, D.,
648 Rosero, E., Tewari, M. and Xia, Y.: The community Noah land surface model with multiparameterization options
649 (Noah-MP): 1. Model description and evaluation with local-scale measurements, *Journal of Geophysical Research*,
650 116(D12), doi:10.1029/2010jd015139, 2011.

651 Parish, T. R.: Forcing of the Summertime Low-Level Jet along the California Coast, *Journal of Applied Meteorology*,
652 39(12), 2421–2433, doi:10.1175/1520-0450(2000)039<2421:fotsll>2.0.co;2, 2000.

653 Rahn, D. A. and Parish, T. R.: Diagnosis of the Forcing and Structure of the Coastal Jet near Cape Mendocino Using
654 In Situ Observations and Numerical Simulations, *Journal of Applied Meteorology and Climatology*, 46(9), 1455–1468,
655 doi:10.1175/jam2546.1, 2007.

656 Rife, D. L., Pinto, J. O., Monaghan, A. J., Davis, C. A. and Hannan, J. R.: Global Distribution and Characteristics of
657 Diurnally Varying Low-Level Jets, *Journal of Climate*, 23(19), 5041–5064, doi:10.1175/2010jcli3514.1, 2010.

658 Saulo, C., Ruiz, J. and Skabar, Y. G.: Synergism between the Low-Level Jet and Organized Convection at Its Exit
659 Region, *Monthly Weather Review*, 135(4), 1310–1326, doi:10.1175/mwr3317.1, 2007.

660 Shapiro, A., Fedorovich, E. and Rahimi, S.: A unified theory for the Great Plains Nocturnal low-level jet, *Journal of*
661 *the Atmospheric Sciences*, 73(8), 3037–3057, doi:10.1175/jas-d-15-0307.1, 2016.

662 Smith, E. N., Gebauer, J. G., Klein, P. M., Fedorovich, E. and Gibbs, J. A.: The Great Plains Low-Level Jet during
663 PECAN: Observed and Simulated Characteristics, *Monthly Weather Review*, 147(6), 1845–1869, doi:10.1175/mwr-
664 d-18-0293.1, 2019.

665 Soares, P. M., Lima, D. C., Semedo, A., Cardoso, R. M., Cabos, W. and Sein, D. V.: Assessing the climate change
666 impact on the North African offshore surface wind and coastal low-level jet using coupled and uncoupled regional
667 climate simulations, *Climate Dynamics*, 52(11), 7111–7132, doi:10.1007/s00382-018-4565-9, 2018.

668 Stensrud, D. J.: Importance of Low-Level Jets to Climate: A Review, *Journal of Climate*, 9(8), 1698–1711,
669 doi:10.1175/1520-0442(1996)009<1698:iolljt>2.0.co;2, 1996.

670 Sullivan, J. T., Rabenhorst, S. D., Dreessen, J., McGee, T. J., Delgado, R., Twigg, L. and Sumnicht, G.: Lidar
671 observations revealing transport of O₃ in the presence of a nocturnal low-level jet: Regional implications for “next-
672 day” pollution, *Atmospheric Environment*, 158, 160–171, doi:10.1016/j.atmosenv.2017.03.039, 2017.

673 Tang, Y., Winkler, J., Zhong, S., Bian, X., Doubler, D., Yu, L. and Walters, C.: Future changes in the climatology of
674 the Great Plains low-level jet derived from fine resolution multi-model simulations, *Scientific Reports*, 7(1),
675 doi:10.1038/s41598-017-05135-0, 2017.

676 Uccellini, L. W., Petersen, R. A., Kocin, P. J., Brill, K. F. and Tuccillo, J. J.: Synergistic Interactions between an
677 Upper-Level Jet Streak and Diabatic Processes that Influence the Development of a Low-Level Jet and a Secondary
678 Coastal Cyclone, *Monthly Weather Review*, 115(10), 2227–2261, doi:10.1175/1520-
679 0493(1987)115<2227:sibaul>2.0.co;2, 1987.

680 Van de Wiel, B. J., Moene, A. F., Steeneveld, G. J., Baas, P., Bosveld, F. C. and Holtslag, A. A.: A conceptual view
681 on inertial oscillations and nocturnal low-level jets, *Journal of the Atmospheric Sciences*, 67(8), 2679–2689,
682 doi:10.1175/2010jas3289.1, 2010.

683 Walters, C. K. and Winkler, J. A.: Airflow Configurations of Warm Season Southerly Low-Level Wind Maxima in
684 the Great Plains. Part I: Spatial and Temporal Characteristics and Relationship to Convection, *Weather and*
685 *Forecasting*, 16(5), 513–530, doi:10.1175/1520-0434(2001)016<0513:acowss>2.0.co;2, 2001.

686 Walters, C. K., Winkler, J. A., Shadbolt, R. P., van Ravensway, J. and Bierly, G. D.: A Long-Term Climatology of
687 Southerly and Northerly Low-Level Jets for the Central United States, *Annals of the Association of American*
688 *Geographers*, 98(3), 521–552, doi:10.1080/00045600802046387, 2008.

689 Weide Luiz, E. and Fiedler, S.: Spatiotemporal observations of nocturnal low-level jets and impacts on wind
690 power production, *Wind Energy Science*, 7(4), 1575–1591, doi:10.5194/wes-7-1575-2022, 2022.

691 Zhang, Y., Xue, M., Zhu, K. and Zhou, B.: What is the main cause of diurnal variation and nocturnal peak of summer
692 precipitation in Sichuan Basin, China? the key role of boundary layer low-level jet inertial oscillations, *Journal of*
693 *Geophysical Research: Atmospheres*, 124(5), 2643–2664, doi:10.1029/2018jd029834, 2019.

694 Zhong, S., Fast, J. D. and Bian, X.: A Case Study of the Great Plains Low-Level Jet Using Wind Profiler Network
695 Data and a High-Resolution Mesoscale Model, *Monthly Weather Review*, 124(5), 785–806, doi:10.1175/1520-
696 0493(1996)124<0785:acsotg>2.0.co;2, 1996.